Journal of Power Sources 195 (2010) 3772–3778

Contents lists available at ScienceDirect

Journal of Power Sources

journal homepage: www.elsevier.com/locate/jpowsour

Novel $SrCo_{1-y}Nb_yO_{3-\delta}$ cathodes for intermediate-temperature solid oxide fuel cells

Fang Wang[a], Qingjun Zhou[a,b], Tianmin He[a,*], Guodong Li[c], Hong Ding[c]

[a] State Key Laboratory of Superhard Materials, and College of Physics, Jilin University, 2699 Qianjin Street Changchun 130012, Jilin, PR China
[b] College of Science, Civil Aviation University of China, Tianjin 300300, PR China
[c] State Key Laboratory of Inorganic Synthesis and Preparative Chemistry, Jilin University, Changchun 130012, PR China

ARTICLE INFO

Article history:
Received 8 December 2009
Received in revised form
17 December 2009
Accepted 17 December 2009
Available online 24 December 2009

Keywords:
Solid oxide fuel cell
Cathode
Strontium cobaltite
Phase transition
Thermal expansion
Electrochemical performance

ABSTRACT

Perovskite oxides $SrCo_{1-y}Nb_yO_{3-\delta}$ (SCN*y*, $y = 0.00–0.20$) are investigated as potential cathode materials for intermediate-temperature solid oxide fuel cells (IT-SOFCs) on $La_{0.9}Sr_{0.1}Ga_{0.8}Mg_{0.2}O_{3-\delta}$ (LSGM) electrolyte. Compared to the undoped $SrCoO_{3-\delta}$, the Nb doping significantly improves the thermal stability and enhances the electrical conductivity of the SCN*y* oxides. The cubic phase of the SCN*y* oxides with high thermal stability can be totally obtained when the Nb doping content $y \geq 0.10$. Among the investigated compositions, the $SrCo_{0.9}Nb_{0.1}O_{3-\delta}$ oxide exhibits the highest electrical conductivity of 461–145 S cm^{-1} over the temperature range of 300–800 °C in air. The SCN*y* cathode has a good chemical compatibility with the LSGM electrolyte for temperatures up to 1050 °C for 5 h. The area specific resistances of SCN*y* with $y = 0.10$, 0.15 and 0.20 cathodes on LSGM electrolyte are 0.083, 0.099 and 0.110 Ω cm^2 at 700 °C, respectively. At $y = 0.10$, 0.15 and 0.20, the maximum power densities of a single-cell with SCN*y* cathodes on 300-μm thick LSGM electrolyte achieve 675, 642 and 625 mW cm^{-2} at 800 °C, respectively. These results indicate that SCN*y* perovskite oxides with cubic phase are potential cathode materials for application in IT-SOFCs.

1. Introduction

Solid oxide fuel cells (SOFCs) represent one of the cleanest, most efficient and versatile power generating technologies that convert chemical energy directly into electrical energy [1,2]. The traditional SOFCs are operated at high temperature (~1000 °C). The high operating temperature can cause complex materials problems, such as electrode sintering and interfacial reaction between electrolyte and electrode materials. It is thus desirable to operate SOFCs at an intermediate-temperature range of around 600–800 °C. A major requirement for the intermediate-temperature-operating SOFCs (IT-SOFCs) is to develop new mixed ionic-electronic conductors (MIECs) as cathode materials with better performance that also fulfill with the cell requirements. The developments of many cathode materials for IT-SOFCs have been reviewed recently by Tsipis and Kharton [3].

Perovskite oxide $SrCoO_{3-\delta}$ is a very important parent compound that can be further developed into many functional materials. The A-site and B-site doped $SrCoO_{3-\delta}$ oxides have been paid much more attention due to their potential and technical applications in oxygen separation membranes, methane conversion reactors and SOFC cathodes [4–13]. The structural evolution research showed that the $SrCoO_{3-\delta}$ oxide exists in three different polymorphs: (i) the orthorhombic "O" brownmillerite phase between room temperature and 653 °C, (ii) the hexagonal "H" phase between 653 and 920 °C, and (iii) the cubic perovskite "C" phase above 920 °C, which is transformed again into the "H" phase at 774 °C when cooled [14]. In the different polymorphs of $SrCoO_{3-\delta}$, high-temperature $SrCoO_{3-\delta}$ phases with cubic 3C-like crystal structures are MIECs, which exhibit the highest electrical conductivity and oxygen permeability values [14,15]. However, the $SrCoO_{3-\delta}$ oxide with 2H $BaNiO_3$-type structure (2H-like hexagonal structure) undergoes phase transitions when it is heated in air. This phase transition causes abrupt changes in the thermal expansion coefficient that would result in cracking problems during the preparation and operation of SOFCs. Moreover, the $SrCoO_{3-\delta}$ oxide with 2H-like hexagonal structure at room temperature was demonstrated to be almost non-oxygen permeable [13,16]. The structural instabilities thus limit this material for further application in oxygen separation devices and SOFCs. Therefore, it is important to inhibit the structural phase transition in $SrCoO_{3-\delta}$, and to stabilize the high-temperature cubic phase to low temperature. In order to stabilize the cubic phase in $SrCoO_{3-\delta}$ oxide, one commonly used method is to dope proper cations for either A-site or B-site to improve the phase stability. Many efforts have been made to stabilize the $SrCoO_{3-\delta}$ cubic perovskite by doping with various elements [6,9,17–20].

* Corresponding author. Tel.: +86 431 88499039; fax: +86 431 88498000.
E-mail addresses: hly@mail.jlu.edu.cn, hetm@jlu.edu.cn (T. He).

0378-7753/$ – see front matter © 2009 Elsevier B.V. All rights reserved.
doi:10.1016/j.jpowsour.2009.12.081

Among these dopant efforts, Nagai et al. [19] demonstrated that Nb was the most effective dopant in $SrCo_{0.9}M_{0.1}O_{3-\delta}$ (M = Cr, Fe, Al, Ga, Ti, Zr, Sn, V and Nb) oxides for improving the phase stability and oxygen permeability. More recently, Zhang et al. [6] systematically investigated new $SrCo_{1-y}Nb_yO_{3-\delta}$ (SCN*y*) ceramic membranes with high oxygen semi-permeability. Their results indicated that the Nb doping content had a significant effect on the phase structure stability, electrical conductivity and oxygen permeability of the $SrCoO_{3-\delta}$ oxides. Moreover, the substitution of Nb for Co in SCN*y* oxides stabilizes the cubic perovskite phase to room temperature at $y \leq 0.2$, thus significantly extends the application scopes of the SCN*y* materials. However, there is little information on the performance of SCN*y* as cathode materials for IT-SOFCs up to date. In this paper, the perovskite oxides $SrCo_{1-y}Nb_yO_{3-\delta}$ (SCN*y*, $y = 0.00–0.20$) were synthesized by a solid-state reaction. The properties of SCN*y* oxides as a potential cathode material were systematically investigated and assessed. The performance of single-cell with SCN*y* cathodes based on $La_{0.9}Sr_{0.1}Ga_{0.8}Mg_{0.2}O_{3-\delta}$ (LSGM) electrolyte was also tested.

2. Experimental

2.1. Sample preparation

The samples SCN*y* ($y = 0.00–0.20$) were synthesized by a solid-state reaction. Stoichiometric amounts of commercial powders $SrCO_3$ (99%), Nb_2O_5 (99%) and Co_3O_4 (99%) were weighed and mixed according to the composition of SCN*y*. The mixed powders were ground thoroughly with ethanol as grinding medium using an agate pestle and mortar. The obtained precursors were then pressed into pellets and calcined repeatedly at 1000, 1100 and 1200 °C for 10 h in air with intermediate grindings, respectively. LSGM and $NiO/Ce_{0.8}Sm_{0.2}O_{1.9}$ (SDC) were used as electrolyte and anode materials in this study, respectively. LSGM, SDC and NiO powders were synthesized using the glycine-nitrate process [21]. The dense LSGM electrolyte pellets were obtained by sintering at 1450 °C for 10 h.

2.2. Characterization

Phase identification of the prepared SCN*y* powders was studied with a Rigaku D/Max 2550 V/PC X-ray diffractometer with Cu Kα radiation ($\lambda = 0.15418$ nm) of 40 kV and 200 mA at room temperature by step scanning in the angle range $20° \leq 2\theta \leq 90°$ with increments of 0.02°. Electrical conductivity of SCN*y* samples were measured in air by the Van der Pauw method using a standard DC voltage/current generator (Cany Precision Instruments, SB118) and a precision digital multimeter (Cany Precision Instruments, PZ158A). Ag paste was used for the electrodes in this measurement. Thermal expansion coefficient (TEC) of SCN*y* samples was measured using a Netzsch DIL 402C dilatometer, which operated in a temperature range from 30 to 1000 °C with an air purge flow rate of 60 ml min^{-1}. Simultaneous differential thermal analysis (DTA) and thermogravimetric analysis (TGA) of SCN*y* samples were investigated on a Netzsch STA 449C thermal analyzer, from 35 to 1000 °C at a heating rate of 10 °C min^{-1} in air with a flowing rate of 50 ml min^{-1}.

Symmetrical cells of SCN*y*/LSGM/SCN*y* ($y = 0.10$, 0.15 and 0.20) for the impedance studies were prepared by screen printing SCN*y* inks onto both sides of the LSGM electrolyte pellet as described previously [22]. After drying, the samples were sintered at 1050 °C for 2 h. AC electrochemical impedance spectroscopy (EIS) was carried out using an electrochemical system (CHI604C, Chenhua) in the temperature range 650–800 °C for all the samples. The frequency of EIS measurement ranged from 0.1 Hz to 100 kHz and signal amplitude of 10 mV was applied. The EIS of the cells was recorded under open circuit voltage (OCV) condition. The single-cell was fabricated by an electrolyte-supported technique with 300-μm-thick LSGM as the electrolyte, NiO-SDC (in a weight ratio of 65:35) as the anode, and SCN*y* ($y = 0.10$, 0.15 and 0.20) as the cathodes. SDC interlayer was introduced between the electrolyte and the anode and sintered at 1300 °C for 1 h. The anode was screen-painted onto the interlayer and then sintered at 1250 °C for 4 h in air. The SCN*y* cathode was painted onto the opposite side of the electrolyte and sintered at 1050 °C for 2 h in air. The single-cell was sealed on one end of an alumina tube with silver paste. The performance of the single-cell was tested using the same electrochemical system with dry hydrogen as fuel and ambient air as oxidant at various temperatures.

3. Results and discussion

3.1. Structural characterization and chemical compatibility

Fig. 1 shows the room-temperature X-ray diffraction (XRD) patterns of SCN*y* samples ($y = 0.00–0.20$) sintered at 1200 °C for 10 h in air through intermediate grinding and calcining at 1000 and 1100 °C. As can be seen from Fig. 1, the XRD pattern of undoped $SrCoO_{3-\delta}$ is quite different from those of SCN*y* samples with $y = 0.05–0.20$. This is further confirmed by the results of electrical property, DTA-TGA and thermal expansion behavior in the following section. The XRD results show that the $SrCoO_{3-\delta}$ oxide crystallize in a hexagonal polymorph, with a distorted 2H $BaNiO_3$-type phase structure. This result is consistent with the data reported by Zhang et al. [6]. While the SCN*y* oxides with $y = 0.05–0.20$ presents a cubic perovskite structure. This indicates that the cubic perovskite phase is efficiently stabilized at room temperature when the SCN*y* oxides are doped with Nb for Co at $y = 0.05–0.20$. With careful observation, it can be found that two weak diffraction peaks at 36.38° and 42.28° are observed in the XRD pattern of the sample with $y = 0.05$, which is indexed as the hexagonal phase. This shows that the SCN*y* oxide with $y = 0.05$ is not fully crystallized into cubic perovskite structure, and is virtually metastable phase. The same phenomena were also observed in the study of SCN*y* oxygen separation membranes [6] and the Ca-doped $SrCoO_{3-\delta}$ system with low Ca doping content [23]. However, no secondary phases are detected by XRD in the case of SCN*y* with $y = 0.10–0.20$, indicating that high purity SCN*y* oxides can be obtained within controlled compositions.

The unit cell volume of SCN*y* in cubic perovskite structure are calculated to be 0.05751(5), 0.05881(5), 0.05901(5) and 0.05936(9) nm^3 for $y = 0.05$, 0.10, 0.15 and 0.20, respectively. It is

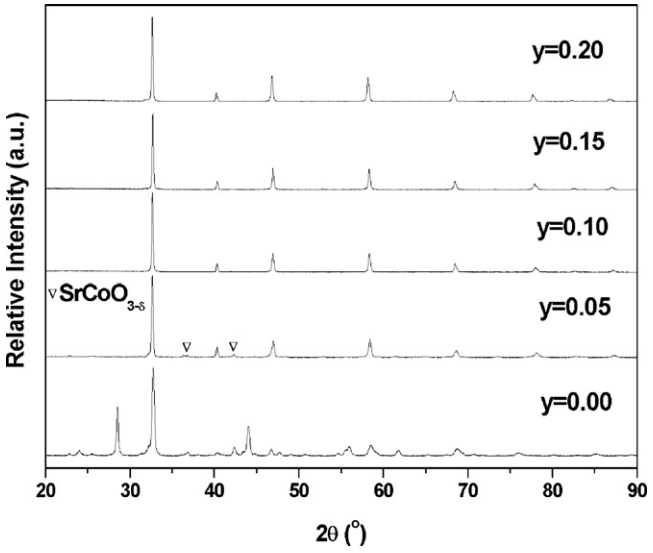

Fig. 1. XRD patterns of samples SCN*y* ($y = 0.00–0.20$) sintered at 1200 °C for 10 h.

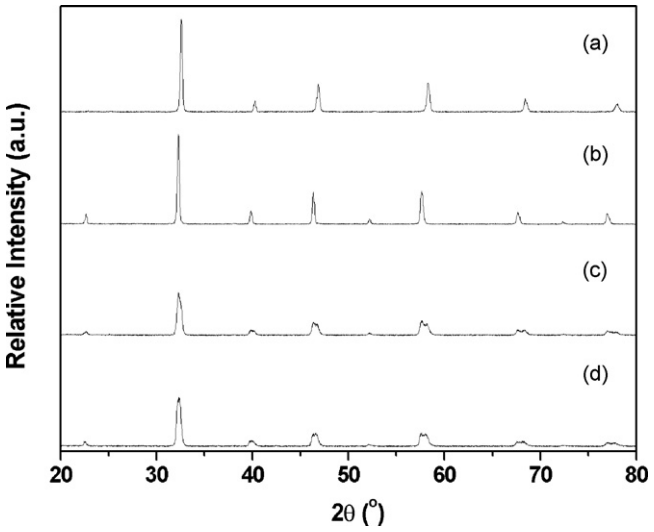

Fig. 2. XRD patterns of (a) SCN*y* ($y = 0.10$) powders, (b) LSGM powders sintered at 1450 °C for 10 h, (c) SCN*y*-LSGM ($y = 0.10$) mixture sintered at 1050 °C for 2 h, and (d) SCN*y*-LSGM ($y = 0.10$) mixture sintered at 1050 °C for 5 h.

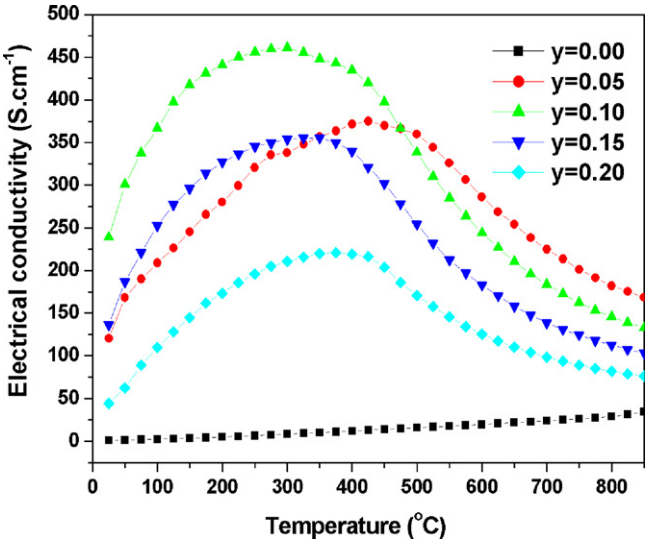

Fig. 3. Temperature dependence of electrical conductivity for samples SCN*y* ($y = 0.00$–0.20) in air, the samples SCN*y* were sintered at 1200 °C for 10 h.

clear that the unit cell volume gradually increases with the increase of the Nb doping content. The Nb^{5+} ions in perovskite are the most common valence state [24]. In SCN*y* oxides, the Nb ion has a fixed valence state of +5, while the valence states of Co ion mostly are +3 or +4 [6]. The ionic radius of Nb^{5+}, Co^{3+} and Co^{4+} is 0.064, 0.061, and 0.053 nm in six-coordination, respectively [25]. The unit cell volume of SCN*y* would gradually increase with the substitution of Nb for Co because the ionic radius of Nb^{5+} is larger than that of Co^{3+} and Co^{4+}.

The interfacial reaction between cathode and electrolyte is highly deleterious, which can increase interfacial polarization resistance, and thus resulting in degradation of the performance of SOFCs. To examine the chemical compatibility between cathode and electrolyte, XRD was used to detect the phase reaction of the SCN*y* cathode with LSGM electrolyte. The mixture of SCN*y* ($y = 0.10$) cathode and LSGM electrolyte powders in a 1:1 weight ratio was sintered at 1050 °C for 2 and 5 h, respectively. Fig. 2 is showing XRD patterns of the SCN*y*, LSGM powders and the SCN*y*-LSGM mixture, respectively. It can be seen from Fig. 2 that no additional reflections and any peak shifts are detected, indicating that there is no significantly chemical reaction between the SCN*y* cathode and LSGM electrolyte. Therefore, this result shows that the SCN*y* cathode is chemically compatible with the LSGM electrolyte for temperatures up to 1050 °C for 5 h.

3.2. Electrical conductivity

Electrical conductivity of a cathode for SOFCs was an important performance indicator. Considerable oxide ion conductivity and sufficient electronic conductivity have been found to be highly beneficial to extend the active oxygen reduction site from the three-phase boundary (TPB) to the whole exposed cathode surface, thus significantly reducing the cathode polarization [26]. In SCN*y* mixed conductors, the total electrical conductivity involves the electronic and the oxygen ionic conductivity. The oxygen ionic conductivity is clearly lower than the electronic conductivity [15]. Therefore the measured conductivity values can be mainly considered as the electronic conductivity. Fig. 3 shows the electrical conductivity behaviors of SCN*y* samples measured in air as a function of temperature. It can be seen from Fig. 3 that, the electrical conductivity property of the undoped $SrCoO_{3-\delta}$ with hexagonal structure is entirely different from those of the SCN*y* with $y = 0.05$–0.20, which exhibits a semiconductor-like behavior. The undoped $SrCoO_{3-\delta}$ has a lower electrical conductivity of 1.2–34 S cm^{-1} between 25 and 850 °C in air, while the electrical conductivity of SCN*y* with $y = 0.05$–0.20 attains 82–360 S cm^{-1} in the temperature range of 500–800 °C. It was demonstrated that the SCN*y* oxides with a cubic perovskite phase revealed the highest electronic and oxygen ionic conductivity [15]. The electrical conductivity of the SCN*y* oxides with $y = 0.05$–0.20 can be greatly enhanced due to the formation of the cubic perovskite phase as demonstrated in XRD results. For an SOFC cathode material, the usual required value for the electrical conductivity is around 100 S cm^{-1} at the operating temperature [27]. Therefore, the electrical conductivity of SCN*y* with cubic perovskite phase as cathode materials is acceptable for application in SOFCs.

For the SCN*y* oxides with $y = 0.05$–0.20, the electrical conductivity of all the SCN*y* samples increases with the increasing temperature and reaches a maximum value in the temperature range of 300–425 °C. This trend presents a semiconductor-like behavior. Thereafter, the electrical conductivity gradually decreases with the further increasing temperature, which is characteristic of metallic-like behavior. This shows that the conduction behavior of the SCN*y* oxides undergoes a change from semiconductor-like to metallic-like occurring around 300–425 °C in the temperature range studied. This can be attributed mainly to the reduction from high valence state Co^{4+} to Co^{3+}, accompanied by the loss of lattice oxygen and the formation of oxygen vacancies [12,28], which is confirmed by thermogravimetric and thermal dilatometric analysis in the following sections, respectively. Below 300–425 °C, the semiconductor-like behavior of SCN*y* samples can be attributed to the hopping conduction mechanism of small polarons, *i.e.*, localized electronic carriers having a thermally activated mobility [29], thus the electrical conductivity increases with increasing temperature. Beyond 300–425 °C, as demonstrated in the following section, the lattice oxygen of SCN*y* samples may be lost at around 300–400 °C, which would result in the formation of oxygen vacancies and the annihilation of holes, as described in Eqs. (1) and (2) according to the defect reaction written in the Kröger-Vink notation

$$O_o^{\times} = V_o^{\bullet\bullet} + 2e' + \frac{1}{2}O_2(g) \quad (1)$$

$$e' + h^{\bullet} = 0 \quad (2)$$

The latter would result in a decrease in the content of holes and hence the electrical conductivity [30]. Furthermore, the change of valence state of Co also causes decrease of the conductivity. In the SCN*y* oxides, the holes are the majority carriers due to the high electronic conductivity [15,31]. The oxygen loss from lattice in the SCN*y* would result in a reduction of content of carriers as described in Eq. (3), thus decreasing the electrical conductivity

$$2Co_{Co}^{\bullet} + O_o^{\times} \Leftrightarrow 2Co_{Co}^{\times} + V_o^{\bullet\bullet} + \frac{1}{2}O_2(g) \quad (3)$$

As can be seen from Fig. 3, the introduction of Nb significantly enhances the electrical conductivity of SCN*y* samples due to the formation of the cubic perovskite phase. The highest electrical conductivity is obtained in $y = 0.10$ sample, which is 461 S cm^{-1} at 300 °C. However, the electrical conductivity decreases with further increase of the Nb doping content. For the perovskite MIECs, simultaneous transport of oxygen ion and electronic conduction was achieved in these oxides. The transport of oxygen ions proceeded through hopping of oxygen vacancies, while transport of electrons was along the B^{n+}–O^{2-}–$B^{(n-1)+}$ network due to overlapping between B:3d and O:2p orbitals [15]. With the increase of Nb doping content, the non-conducting Nb–O bonds increase, which obstructs the electronic transport [12], thus the electrical conductivity is decreased.

3.3. Thermal expansion behavior

Fig. 4(a) shows the thermal expansion curves of the SCN*y* samples over a temperature range of 30–1000 °C in air. The thermal expansion curve of undoped $SrCoO_{3-\delta}$ sample is significantly different from those of other samples for $y = 0.05$–0.20. As demonstrated in the above XRD result, the $SrCoO_{3-\delta}$ oxide is a 2H $BaNiO_3$-type phase structure, which has three different polymorphs from room temperature to 1200 °C [14]. That is, the orthorhombic phase between room temperature and 653 °C, the hexagonal phase between 653 and 920 °C, and the cubic perovskite above 920 °C. To reveal more clearly difference of the phase temperature in the SCN*y* samples, differential curves of $\Delta L/L_0$ *vs.* temperature for SCN*y* samples are shown in Fig. 4(b). One abrupt change at 920 °C appears in the differential curve for undoped $SrCoO_{3-\delta}$ sample, which corresponds to the hexagonal to cubic structural phase transition [14]. Similarly, a small abrupt change is also detected for the sample with $y = 0.05$, indicating that there is still existence of the structural phase transition mentioned above. This is in very good agreement with the XRD analysis, in which the sample with $y = 0.05$ is a metastable phase due to existence of a small amount of hexagonal phase. And the phase transition temperature shifts toward low temperature at about 905 °C. However, no structural phase transition is observed at about 920 °C for all Nb-doped samples when $y \geq 0.10$. This means that the structural phase transition in SCN*y* oxides can be inhibited completely as Nb doping content is more than 0.10. This result is consistent with the XRD results discussed above. The thermal expansion behavior results show that the samples for $y = 0.00$ and 0.05 are structurally unstable at around 920 and 905 °C in air, which may result in delamination and crack of the cathodes from the electrolytes during the preparation and sintering of fuel cell. Therefore, the two samples are unsuitable for use as a cathode material in SOFCs. Other samples with $y = 0.10$–0.20 can be considered as a cathode material for SOFCs due to no structural phase transition in the temperature range investigated. In addition, a change of the slope appears at around 400 °C in the thermal expansion curves for the samples SCN*y* with $y = 0.10$–0.20, which can be associated with the reduction from high valence state Co^{4+} to Co^{3+} and the loss of lattice oxygen as demonstrated by DTA-TGA results. The related defect reaction has been expressed in Eq. (3). Similar results have been reported in

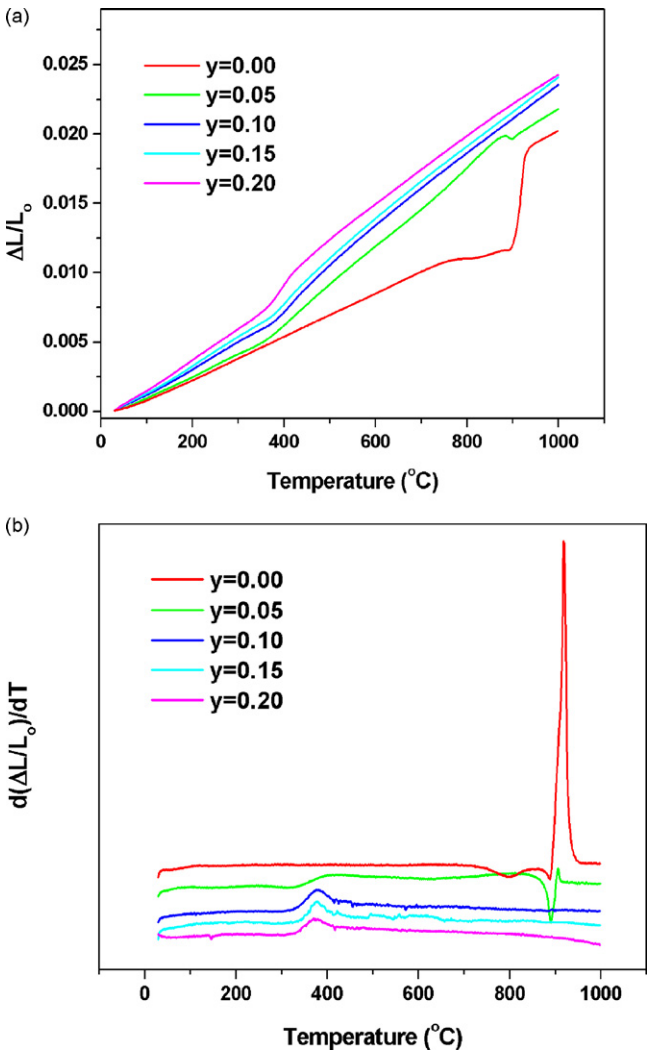

Fig. 4. (a) Thermal expansion curves of samples SCN*y* ($y = 0.00$–0.20) between 30 and 1000 °C in air, and (b) Differential curves of $\Delta L/L_0$ *vs.* temperature for samples SCN*y*.

the $SrCo_{1-x}Sb_xO_{3-\delta}$ and $Ba_{0.5}Sr_{0.5}Co_{0.8}Fe_{0.2}O_{3-\delta}$ perovskite oxides [12,27]. As discussed in Section 3.1, the ionic radius of Co^{3+} and Co^{4+} is 0.061 and 0.053 nm, respectively [25]. The valence change of Co from Co^{4+} to Co^{3+} would introduce more Co^{3+}, leading to the lattice expansion and thus the high thermal expansion behaviors.

The TECs of samples SCN*y* ($y = 0.10$–0.20) increase with the increase of the Nb doping content. The TEC values are 24.2×10^{-6}, 24.5×10^{-6} and 24.9×10^{-6} K^{-1} for $y = 0.10$, 0.15 and 0.20, respectively, which is consistent with the usual relationship that the larger unit cell volume corresponds to larger TEC for the same crystal structure [32]. We can see that the unit cell volume of SCN*y* compositions increases from 0.05881(5) nm^3 for $y = 0.10$ to 0.05936(9) nm^3 for $y = 0.20$. Therefore, the TECs of the SCN*y* samples exhibit an increasing tendency with the increase of the Nb doping content.

3.4. DTA and TGA

To examine the thermal stability of the SCN*y* oxides, simultaneous DTA and TGA measurements were carried out over a temperature range of 35–1000 °C in air. Fig. 5(a) and (b) shows the DTA and TGA curves of SCN*y* samples during heating pro-

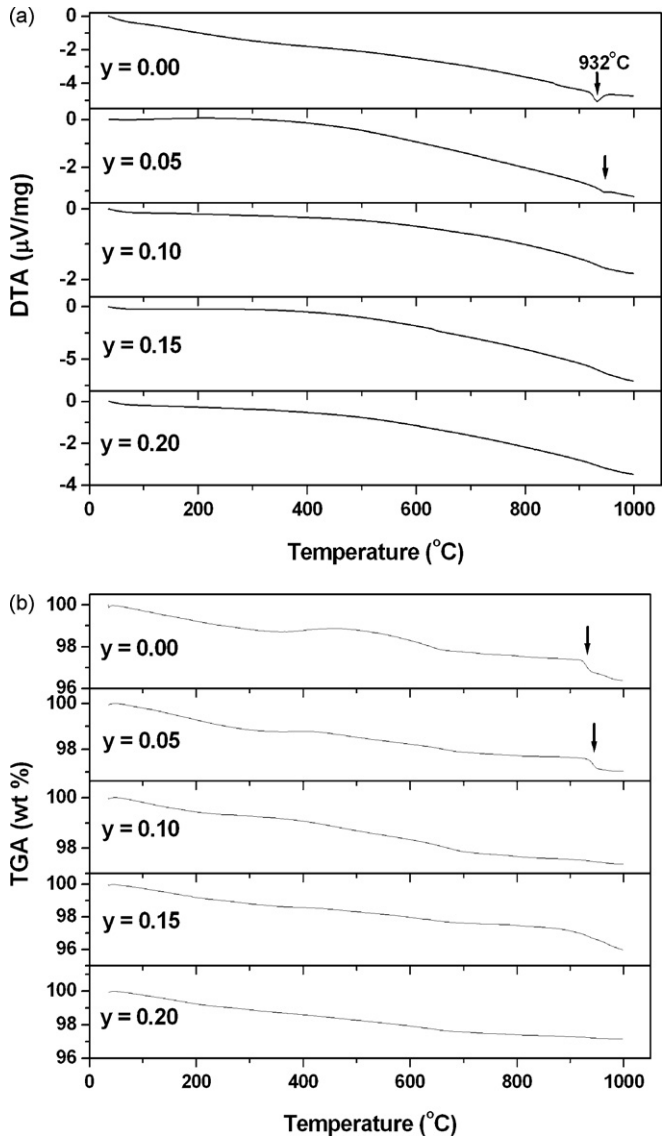

Fig. 5. (a) DTA and (b) TGA curves of samples SCN*y* ($y = 0.00$–0.20) in the temperature range of 35–1000 °C in air.

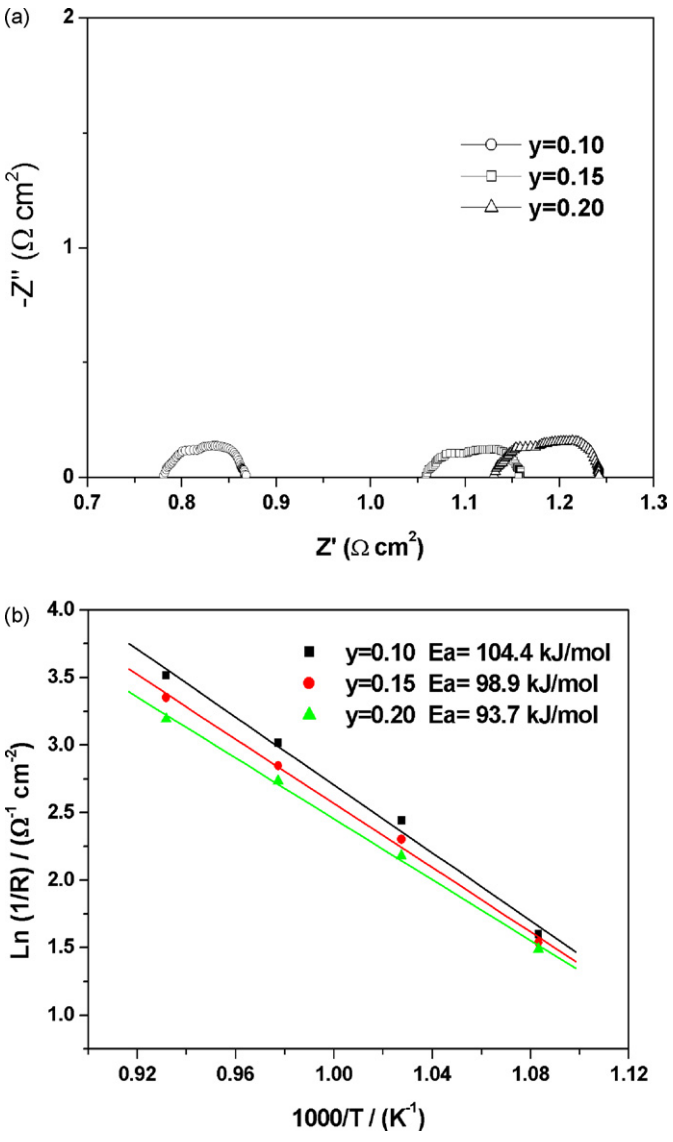

Fig. 6. (a) Typical impedance spectra of SCN*y* ($y = 0.00$–0.20) cathodes on LSGM electrolyte measured at 700 °C, and (b) Arrhenius plots of ASR values for SCN*y* cathodes.

cess, respectively. For all the samples, the DTA and TGA curves decrease monotonously with temperature. A significant weight loss occurs at above 300 °C in TGA curves due to the loss of oxygen from the lattice [28,31,33], as described in Eq. (3). This result agrees with the results of the thermal expansion behavior and the electrical conductivity. When the temperature is increased up to around 930 °C, a sharp and weak endothermic peak are observed in DTA curves of the $SrCoO_{3-\delta}$ and $SrCo_{0.95}Nb_{0.05}O_{3-\delta}$ samples, respectively. Simultaneously, a visible weight loss also is observed in TGA curves at this temperature for the two samples. This change in the samples of $SrCoO_{3-\delta}$ and $SrCo_{0.95}Nb_{0.05}O_{3-\delta}$ corresponds to a structural phase transition from hexagonal to cubic phase. This result is consistent with the study of thermal expansion behaviors discussed in Section 3.3. However, no visible change at around 930 °C is observed in the DTA and TGA curves for SCN*y* samples with $y = 0.10$–0.20. This suggests that substitution of Nb for Co have fully stabilized the cubic perovskite structure of SCN*y* oxides at $0.10 \le y \le 0.20$. Therefore, the Nb doping content y should be selected between 0.10 and 0.20 from the viewpoint of an operating stability of SCN*y* cathode for application in SOFCs.

3.5. Area specific resistance

The area specific resistance (ASR) represents the overall cathodic properties related to oxygen reduction, oxygen surface/bulk diffusion and gas-phase oxygen diffusion [34]. To assess the electrochemical activities of the SCN*y* cathodes, the impedance spectroscopy of the symmetrical cells was investigated under open-current conditions from 650 to 800 °C. Fig. 6(a) shows the typical impedance spectra of SCN*y*/LSGM/SCN*y* symmetrical cells for SCN*y* cathodes with $y = 0.10$–0.20 measured at 700 °C in air. For all the SCN*y* samples, the impedance response on the SCN*y* cathodes is characterized by two visibly separable arcs at high-frequency and low-frequency, indicating that there are at least two electrode processes in the oxygen reduction reaction on the SCN*y* cathodes. The high-frequency intercept of the impedance spectra represents the ohmic resistance of the electrolyte, electrodes and connection wires, while the difference between the high-frequency and low-frequency intercepts on the impedance spectra corresponds to the ASR of the two interfaces [35]. The ASR values for SCN*y* cathodes with temperature are shown in Table 1. The ASR of SCN*y* cathodes increases with the Nb content from $y = 0.10$ to $y = 0.20$. This

Table 1
ASR data for SCN*y* cathodes on LSGM electrolyte.

Temperature (°C)	10%Nb (Ω cm^2)	15%Nb (Ω cm^2)	20%Nb (Ω cm^2)
650	0.210	0.214	0.226
700	0.083	0.099	0.110
750	0.049	0.057	0.065
800	0.029	0.033	0.040

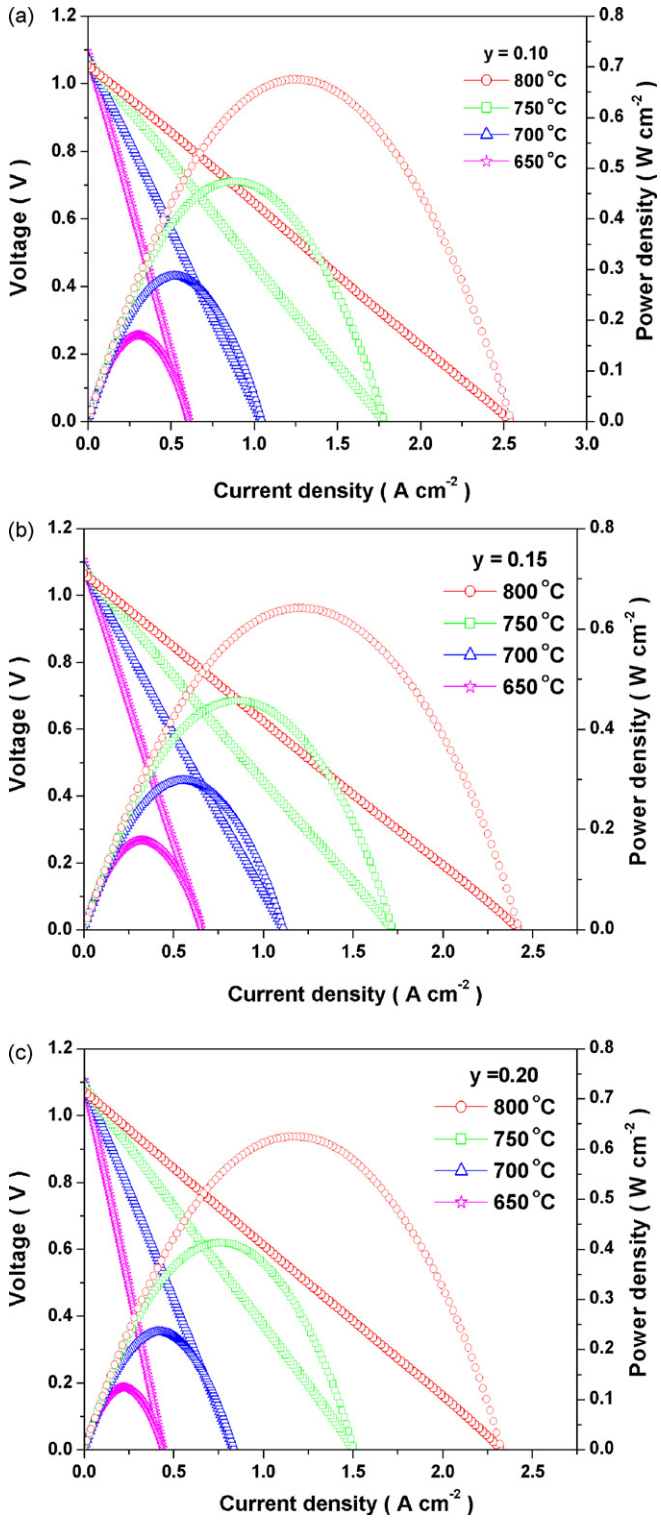

Fig. 7. Cell voltage and power density as a function of current density for a Ni-SDC/SDC/LSGM/SCN*y* cell measured at 650–800 °C using dry H_2 as fuel and ambient air as oxidant: (a) $y = 0.10$, (b) $y = 0.15$ and (c) $y = 0.20$.

is mainly attributable to the reduction of oxygen vacancy content in SCN*y* oxides. As discussed in Section 3.2, the transport of oxygen ions proceeded *via* hopping of oxygen vacancies [15]. The introduction of Nb^{5+} into the $SrCoO_{3-\delta}$ causes a reduction of oxygen vacancy content [19]. Also the oxygen vacancy content decreases with the increase of Nb doping content in SCN*y*, thus leading to a decrease of the oxygen reduction reaction. This result is supported by the research made by Zhang et al. [6], in which the oxygen vacancy of samples SCN*y* decreased with Nb doping content. For example, the oxygen vacancy reduced from 0.147(2) for $y = 0.10$ to 0.043(4) for $y = 0.20$. However, the ASR values of all the samples are lower than 0.110 Ω cm^2 at 700 °C, which is lower than an expected criterion (0.15 Ω cm^2) for the ASR of the cathode [36]. Therefore, the results indicate that the SCN*y* cathodes have a higher electrocatalytic activity for oxygen reduction reactions at intermediate temperatures, and hence the better cathode performance. Fig. 6(b) shows Arrhenius plots of the ASR values for SCN*y* cathodes. The activation energy calculated from the slope of Fig. 6(b) is 104.4, 98.9 and 93.7 kJ mol^{-1}. This result is lower than those for double-perovskite structure cathode $SmBaCo_2O_{5+x}$ (SBCO) [22] and their composite cathodes [37] in our previous reports. For example, the activation energies were 111.1 and 120.8 kJ mol^{-1} for the SBCO cathode on LSGM and SDC electrolytes, respectively.

3.6. Single-cell performance

Fig. 7(a)–(c) shows cell voltage and power density as a function of current density for the Ni-SDC/SDC/LSGM/SCN*y* cell with cathodes $y = 0.10$, 0.15 and 0.20, respectively. The cell was tested using dry H_2 as fuel and ambient air as oxidant in the temperature range of 650–800 °C. At 800 °C, the maximum power density values of cell achieve 678, 642 and 625 mW cm^{-2} for SCN*y* cathodes with the change from $y = 0.10$ to 0.20, respectively. This result is consistent with the ASR data mentioned above. High power densities demonstrate that SCN*y* oxides are promising cathode materials for IT-SOFCs. In addition, the cell with SCN*y* cathode of $y = 0.10$ presents a more excellent performance as compared to SCN*y* cathode with $y = 0.15$ and 0.20. Therefore, the SCN*y* cathode with $y = 0.10$ is preferred for application in IT-SOFCs.

4. Conclusions

In this study, the $SrCo_{1-y}Nb_yO_{3-\delta}$ (SCN*y*, $y = 0.00$–0.20) series oxides were synthesized by a solid-state reaction and the selected compositions were investigated as a potential cathode material for IT-SOFCs. The Nb doping content had a significant effect on the phase structure stability, electrical conductivity and electrochemical performance of the SCN*y* oxides. A fully stable and cubic perovskite structure could be obtained for the SCN*y* compositions with $y = 0.10$–0.20. Among the studied compositions, the SCN*y* cathode with $y = 0.10$ presented the highest electrical conductivity and electrochemical performance. At $y = 0.10$, 0.15 and 0.20, the electrical conductivity of SCN*y* oxides attained 244–145, 183–112 and 125–82 S cm^{-1} in the temperature range of 600–800 °C, respectively. The ASR values for the SCN*y* cathodes on LSGM electrolyte were 0.083, 0.099 and 0.110 Ω cm^2 at 700 °C, respectively. The maximum output power density of a single-cell with SCN*y* cathodes attained 678, 642 and 625 mW cm^{-2} at 800 °C, respectively. These results indicated that the SCN*y* oxides with $y = 0.10$–0.20 were very promising candidates to be used as cathode materials for IT-SOFCs. The SCN*y* cathode of $y = 0.10$ is preferred in view of its excellent performance compared to SCN*y* cathode of $y = 0.15$ and 0.20.

Acknowledgement

This work was supported by the Natural Science Foundation of China under contract No. 10974065.

References

[1] N.Q. Minh, J. Am. Ceram. Soc. 76 (1993) 563–588.
[2] B.C.H. Steele, Solid State Ionics 129 (2000) 95–110.
[3] E.V. Tsipis, V.V. Kharton, J. Solid State Electrochem. 12 (2008) 1367–1391.
[4] V.V. Kharton, A.A. Yaremchenko, A.V. Kovalevsky, A.P. Viskup, E.N. Naumovich, P.F. Kerko, J. Membr. Sci. 163 (1999) 307–317.
[5] P.Y. Zeng, R. Ran, Z.H. Chen, H.X. Gu, Z.P. Shao, AIChE J. 53 (2007) 3116–3124.
[6] K. Zhang, R. Ran, L. Ge, Z.P. Shao, W.Q. Jin, N.P. Xu, J. Membr. Sci. 323 (2008) 436–443.
[7] K. Zhang, R. Ran, L. Ge, Z.P. Shao, W.Q. Jin, N.P. Xu, J. Alloys Compd. 474 (2009) 477–483.
[8] P.Y. Zeng, Z.P. Shao, S.M. Liu, Z.P. Xu, Sep. Purif. Technol. 67 (2009) 304–311.
[9] P.Y. Zeng, R. Ran, Z.H. Chen, W. Zhou, H.X. Gu, Z.P. Shao, S.M. Liu, J. Alloys Compd. 455 (2008) 465–470.
[10] Y.P. Li, E.R. Maxey, J.W. Richardson, J. Am. Ceram. Soc. 88 (2005) 1244–1252.
[11] A. Aguadero, C. de la Calle, J.A. Alonso, M.J. Escudero, M.T. Fernández-Díaz, L. Daza, Chem. Mater. 19 (2007) 6437–6444.
[12] A. Aguadero, D. Pérez-Coll, C. de la Calle, J.A. Alonso, M.J. Escudero, L. Daza, J. Power Sources 192 (2009) 132–137.
[13] B. Lin, S.L. Wang, H.L. Liu, K. Xie, H.P. Ding, M.F. Liu, G.Y. Meng, J. Alloys Compd. 472 (2009) 556–558.
[14] C. de la Calle, A. Aguadero, J.A. Alonso, M.T. Fernández-Díaz, Solid State Sci. 10 (2008) 1924–1935.
[15] Z.Q. Deng, W.S. Yang, W. Liu, C.S. Chen, J. Solid State Chem. 179 (2006) 362–369.
[16] H. Kruidhof, H.J.M. Bouwmeester, R.H.E.V. Doorn, A.J. Burggraaf, Solid State Ionics 816 (1993) 63–65.
[17] M. James, D. Cassidy, K.F. Wilson, J. Horvat, R.L. Withers, Solid State Sci. 6 (2004) 655–662.
[18] X.L. Dong, Z. Xu, X.F. Chang, C. Zhang, W.Q. Jin, J. Am. Ceram. Soc. 90 (2007) 3923–3929.
[19] T. Nagai, W. Ito, T.R. Sakon, Solid State Ionics 177 (2007) 3433–3444.
[20] W. Ito, T. Nagai, T. Sakon, Solid State Ionics 178 (2007) 809–816.
[21] L.G. Cong, T.M. He, Y. Ji, P.F. Guan, Y.L. Huang, W.H. Su, J. Alloys Compd. 348 (2003) 325–331.
[22] Q.J. Zhou, T.M. He, Y. Ji, J. Power Sources 185 (2008) 754–758.
[23] N. Miura, H. Murae, H. Kusaba, J. Tamaki, G. Sakai, N. Yamazoe, J. Electrochem. Soc. 146 (1999) 2581–2586.
[24] V.V. Atuchin, I.E. Kalabina, V.G. Kesler, N.V. Pervukhina, J. Electron. Spectrosc. Relat. Phenom. 142 (2005) 129–134.
[25] R.D. Shannon, Acta Crystallogr. A32 (1976) 751–767.
[26] W. Zhou, R. Ran, Z.P. Shao, J. Power Sources 192 (2009) 231–246.
[27] E. Boehm, J.-M. Bassat, M.C. Steil, P. Dordor, F. Mauvy, J.-C. Grenier, Solid State Sci. 5 (2003) 973–981.
[28] B. Wei, Z. Lü, S. Li, Y. Liu, K. Liu, W. Su, Electrochem. Solid State Lett. 8 (2005) A428–A431.
[29] J.W. Stevenson, T.R. Armstrong, R.D. Carneim, L.R. Pederson, W.J. Weber, J. Electrochem. Soc. 143 (1996) 2722–2729.
[30] H. Zhao, W. Shen, Z. Zhu, X. Li, Z. Wang, J. Power Sources 182 (2008) 503–509.
[31] L.W. Tai, M.M. Nasrallah, H.U. Anderson, D.M. Sparlin, S.R. Sehlin, Solid State Ionics 76 (1995) 259–271.
[32] H. Hayashi, M. Watanabe, M. Ohuchida, H. Inaba, Y. Hiei, T. Yamamoto, M. Mori, Solid State Ionics 144 (2001) 301–313.
[33] G.Ch. Kostogloudis, N. Vasilakos, Ch. Ftikos, Solid State Ionics 106 (1998) 207–218.
[34] S.W. Baek, J.H. Kim, J. Bae, Solid State Ionics 179 (2008) 1570–1574.
[35] E.P. Murray, S.A. Barnett, Solid State Ionics 143 (2001) 265–273.
[36] B.C.H. Steele, Solid State Ionics 86–88 (1996) 1223–1234.
[37] Q. Zhou, F. Wang, Y. Shen, T. He, J. Power Sources 195 (2010) 2174–2181.